

Supplementary Material for

The Impacts of Fossil Fuel Emission Uncertainties and Accounting for 3-D Chemical CO₂ Production on Inverse Natural Carbon Flux Estimates from Satellite and In Situ Data

James S. Wang, Tomohiro Oda, S. Randolph Kawa, Sarah A. Strode, David F. Baker, Lesley E. Ott, Steven Pawson

Methods: Additional details

The MERRA2-GMI output is available at a resolution of $0.5^\circ \times 0.625^\circ$. The GMI chemical mechanism includes 122 species, 321 thermal reactions, and 81 photolysis reactions. GMI calculates photolysis rates using an updated version of Fast-JX (*Wild et al., 2000; Bian and Prather, 2002*). CO is oxidized by OH and methane oxidation occurs by reactions with OH, O(¹D), and Cl. The monthly and interannually varying emissions of reactive gases for MERRA2-GMI are derived from various sources, including MACCity for fossil fuel and biofuel emissions (*Granier et al., 2011*), GFED4 for biomass burning (*van der Werf et al., 2017*), and internally calculated, meteorology-dependent, terrestrial, biogenic NMVOCs including isoprene, propene, and CO from methanol and monoterpene oxidation (*Guenther et al., 1999, 2000*). Emissions of CH₄ are not explicitly simulated in MERRA2-GMI; rather, spatiotemporally varying surface-layer boundary conditions are prescribed.

For the chemical pump surface correction, we do not subtract fossil CH₄ emissions, since the baseline FFCO₂ emissions do not include fugitive CH₄ emissions and CH₄ is not a significant product of fossil fuel combustion. Unlike *Nassar et al. (2010)*, we implement a correction for biomass and biofuel burning (see Table 1) since our baseline GFED emissions include all carbon species, not just CO₂. For that correction, we apply a total non-CO₂ emission factor from GFED averaged over ecosystem types, 0.10, to the total biomass and biofuel burning emissions. For biospheric CH₄, we adopt the termite and interannually varying wetland and rice paddy sources from the TransCom-CH₄ study (*Patra et al., 2011*). Unlike previous studies, we omitted ruminant and landfill CH₄ sources, totaling ~ 0.1 Pg C yr⁻¹, primarily for practical reasons.

Note that for this surface correction, we subtract for simplicity the entire amount of reduced carbon emissions rather than just the portion that is eventually oxidized to CO; in contrast, *Suntharalingam et al. (2005)*, for example, used equivalent CO emissions corresponding to NMVOCs with yields ranging from 0.2 to 1. To compensate for the resulting imbalance between chemical CO₂ production and surface correction, we apply simple adjustments to the inversion flux results after the fact; specifically, we subtract amounts from the regional posterior fluxes that are proportional to the total surface correction in each region (thus affecting land regions mostly) and that sum up to the global imbalance. The adjustments are in any case relatively small, as the global imbalance is only -0.11 Pg C yr⁻¹ (Table 1).

Possible shortcomings of the MERRA2-GMI simulation that could affect our prescribed CO loss rates and surface correction include a low bias in northern hemisphere CO relative to observations (Strode et al, 2015; Strode et al., 2016) that is also found in many other global models (e.g. Naik et al., 2013), an excessive Northern Hemisphere/Southern Hemisphere ratio of OH abundance relative to observation-based estimates—possibly causally connected to the CO bias, with a ratio of 1.26 (for 2007) compared to values of 0.85-0.98 (Naik et al 2013; Patra et al 2014), and emissions of biogenic isoprene that are likely too high compared to that of, e.g., Guenther et al (1999, 2000). But the objective of our study was to assess possible impacts to CO₂ flux inversions rather than providing the most accurate quantitative results.

Results: Analysis of posterior fit to observations

We examine the posterior fit of the inversions to observations to assess whether that could provide an objective rationale for accounting for bunker emissions and the chemical pump in CO₂ inversions. One measure of the goodness of fit to assimilated observations is the value of the cost function that is minimized in a Bayesian inversion (defined in Eq. 2 of Wang et al., 2018). Prior and posterior values of the cost function are shown for different inversions in Table S1. Part of the reason the prior values are large is that the terrestrial biosphere is assumed to be near neutral while in reality it is thought to generally be a net CO₂ sink; the addition of bunker emissions further increases the global budget discrepancy and thus the "cost." Although the prior values of the cost function vary substantially among the different cases (with ODIAC land-based emissions, ODIAC land-based and bunker emissions, and ODIAC and chemical pump), the posterior fit differs little among the cases for either the in situ or GOSAT inversions. Interestingly, there are somewhat larger differences in the posterior cost function values between the CDIAC- and ODIAC-based inversions, with the latter exhibiting tighter fits to the observations (Table S1).

We also evaluate the inversions against independent data as well as the assimilated data. In one analysis, we evaluate the in situ inversion against the GOSAT data as well as the in situ data, and vice versa. Histograms of model minus observation values exhibit only slight differences among different cases—CDIAC, ODIAC land, ODIAC with bunkers, and ODIAC with chemical pump (not shown). In another analysis, we consider biweekly aircraft measurements of CO₂ vertical profiles from near-surface to 4.4 km over four sites across the Amazon (Gatti et al., 2014, 2016), which are presumably sensitive to 3-D chemical CO₂ production and the biospheric surface corrections (Fig. S1a). Although there are sizable differences in the prior agreement with the observations with and without the chemical pump, the posterior agreement for the GOSAT inversions is similar overall, as indicated by model – observation histograms (Fig. S2). Individual model profiles also exhibit slight differences in general, with no clear seasonal patterns, e.g., dry vs. wet season (not shown). The in situ inversion, on the other hand, appears to exhibit a closer fit to the observations when the chemical pump is included (Fig. S2). However, given that the in situ inversion is severely under-

constrained in the Amazon (Wang et al., 2018), the results here probably reflect an influence from the prior, which exhibits a closer fit to the observations when the chemical pump is included.

In summary, although accounting for international bunkers and the chemical pump changes the prior atmospheric CO₂ distributions, the inversion adjustments appear to be able to produce a similar fit to various observations, except in regions where the inversion is under-constrained. The posterior *fluxes* differ for the different cases though.

References

- Bian, H., and M. J. Prather (2002), Accurate simulation of stratospheric photolysis in global chemical model, *J. Atmos. Chem.*, **41**, 281-296.
- Gatti L V *et al* 2014 Drought sensitivity of Amazonian carbon balance revealed by atmospheric measurements *Nature* **506** 76-80
- Gatti, L., Gloor, E., and Miller, J.: Greenhouse gas profile measurements (CO, CO₂, CH₄) above the forest canopy at four sites for the Amazonica project. NCAS British Atmospheric Data Centre, accessed 5 Dec 2016.
<http://catalogue.ceda.ac.uk/uuid/7201536a8b7a1a96de584e9b746acee3>, 2016.
- Granier C *et al* 2011 Evolution of anthropogenic and biomass burning emissions of air pollutants at global and regional scales during the 1980-2010 period *Climatic Change* **109** 163-190
- Guenther A, Baugh B, Brasseur G, Greenberg J, Harley P, Klinger L, Serça D and Vierling L 1999 Isoprene emission estimates and uncertainties for the central African EXPRESSO study domain *J. Geophys. Res. Atmos.* **104** 30625-30639
- Guenther A 2000 Natural emissions of non-methane volatile organic compounds, carbon monoxide, and oxides of nitrogen from North America *Atmospheric Environment* **34** 2205-2230
- Naik V *et al* 2013 Preindustrial to present-day changes in tropospheric hydroxyl radical and methane lifetime from the Atmospheric Chemistry and Climate Model Intercomparison Project (ACCMIP) *Atmos. Chem. Phys.* **13** 5277–5298
- Nassar R *et al* 2010 Modeling global atmospheric CO₂ with improved emission inventories and CO₂ production from the oxidation of other carbon species *Geosci. Model Dev.* **3** 689–716
- Patra P, Houweling S, Krol M, Bousquet P, Belikov D, et al. 2011. TransCom model simulations of CH₄ and related species: linking transport, surface flux and chemical loss with CH₄ variability in the troposphere and lower stratosphere. *Atmospheric Chemistry and Physics* **11**(24): 12813-12837
- Patra P K *et al* 2014 Observational evidence for interhemispheric hydroxyl-radical parity *Nature* **513** 219–223

- Strode S, Duncan B, Yegorova E, Kouatchou J, Ziemke J, et al. 2015. Implications of carbon monoxide bias for methane lifetime and atmospheric composition in chemistry climate models. *Atmospheric Chemistry and Physics* **15**(20): 11789-11805
- Strode, S. A., Worden, H. M., Damon, M., Douglass, A. R., Duncan, B. N., Emmons, L. K., Lamarque, J.-F., Manyin, M., Oman, L. D., Rodriguez, J. M., Strahan, S. E., and Tilmes, S.: Interpreting space-based trends in carbon monoxide with multiple models, *Atmos. Chem. Phys.*, 16, 7285–7294, <https://doi.org/10.5194/acp-16-7285-2016>, 2016.
- Suntharalingam, P., J. T. Randerson, N. Krakauer, J. A. Logan, and D. J. Jacob 2005 Influence of reduced carbon emissions and oxidation on the distribution of atmospheric CO₂: Implications for inversion analyses *Global Biogeochem. Cycles* **19** GB4003
- van der Werf G R *et al* 2017 Global fire emissions estimates during 1997–2016 *Earth Syst. Sci. Data* **9** 697-720
- Wang, J. S., Kawa, S. R., Collatz, G. J., Sasakawa, M., Gatti, L. V., Machida, T., Liu, Y., and Manyin, M. E.: A global synthesis inversion analysis of recent variability in CO₂ fluxes using GOSAT and in situ observations, *Atmos. Chem. Phys.*, 18, 11097–11124, doi:10.5194/acp-18-11097-2018, 2018.
- Wild, O., X. Zhu, and M. Prather (2000), Fast-J: Accurate simulation of in- and below-cloud photolysis in tropospheric chemical models, *J. Atmos. Chem.* **37**, 245-282.

Table S1. Normalized Cost Function Values for Inversions.

Inversion	A priori	A posteriori
In situ		
With CDIAC	112.4	4.0
With ODIAC (land)	124.407	3.870
With ODIAC + 3D bunkers	139.863	3.873
With ODIAC + 3D bunkers + 3D chem	135.072	3.867
GOSAT		
With CDIAC	2.2	0.8
With ODIAC (land)	2.372	0.778
With ODIAC + 3D bunkers	2.659	0.778
With ODIAC + 3D bunkers + 3D chem	2.551	0.777

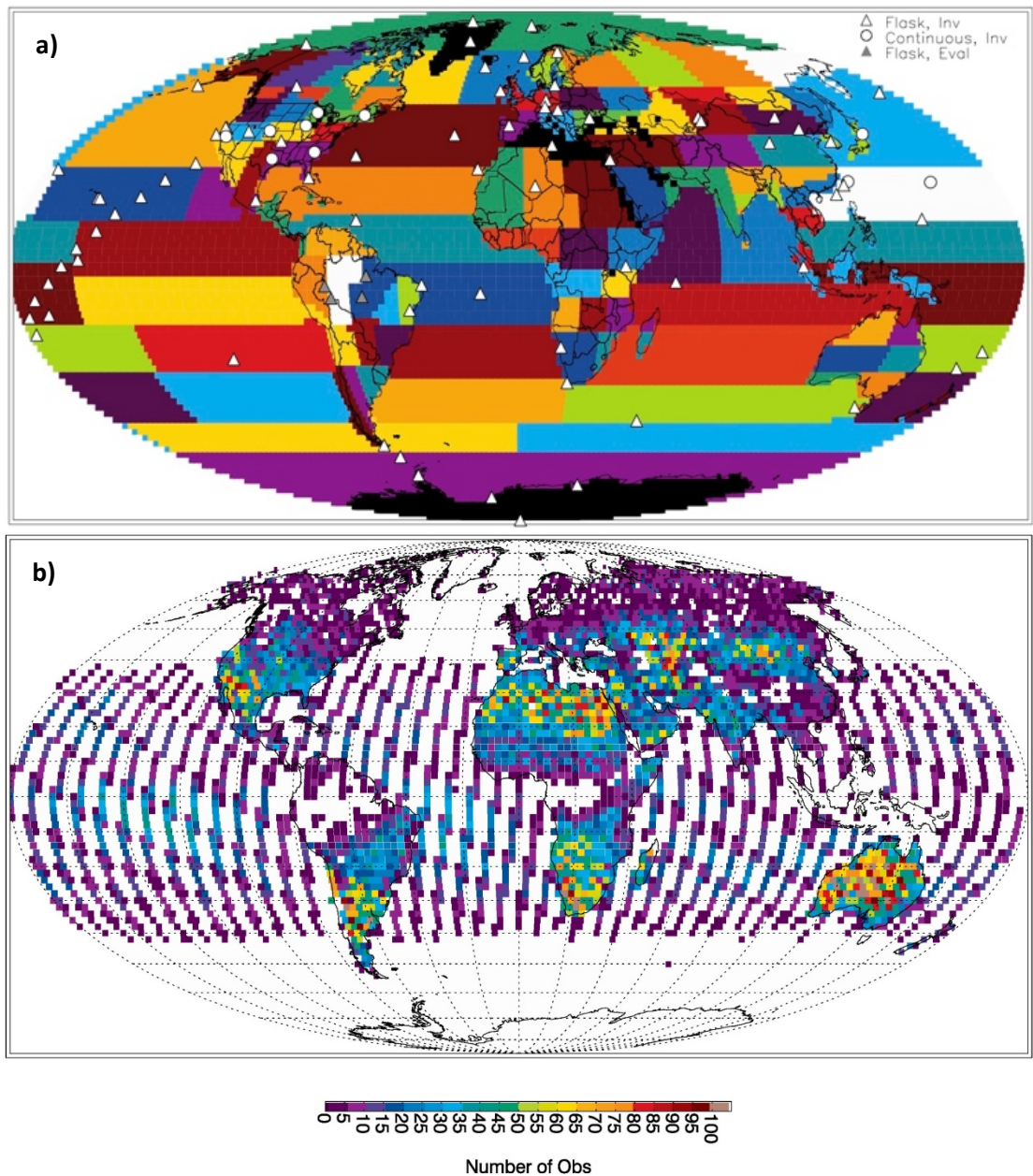
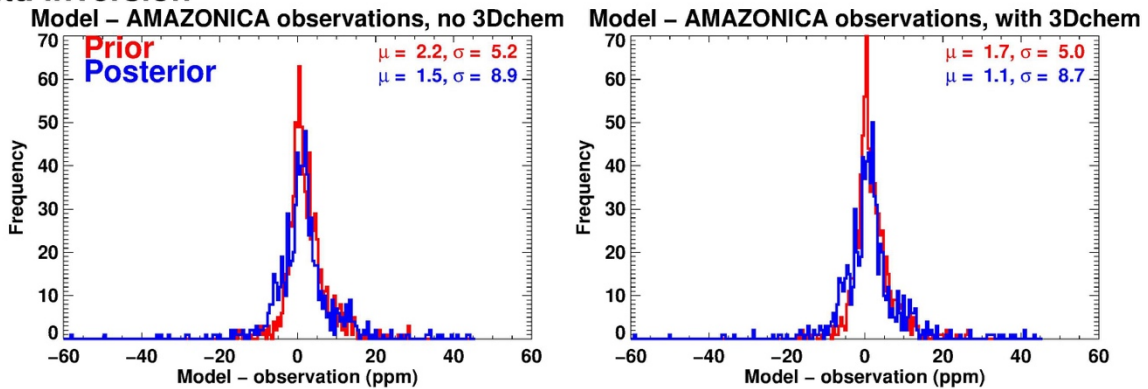


Figure S1. Locations of a) in situ observation sites and b) GOSAT XCO₂ observations used in the inversions. Also shown in a) are the 108 flux regions. Flask and continuous measurement sites in a) are represented by different symbols, and sites used in inversions and in their evaluation are represented by different colors. Observations in b) correspond to the ACOS B3.4 retrieval, are filtered and averaged over each hour and 2° x 2.5° PCTM model grid column, and are shown for June 2009-May 2010. Adapted from Wang et al. (2018) CC BY 4.0.

In situ inversion



GOSAT inversion

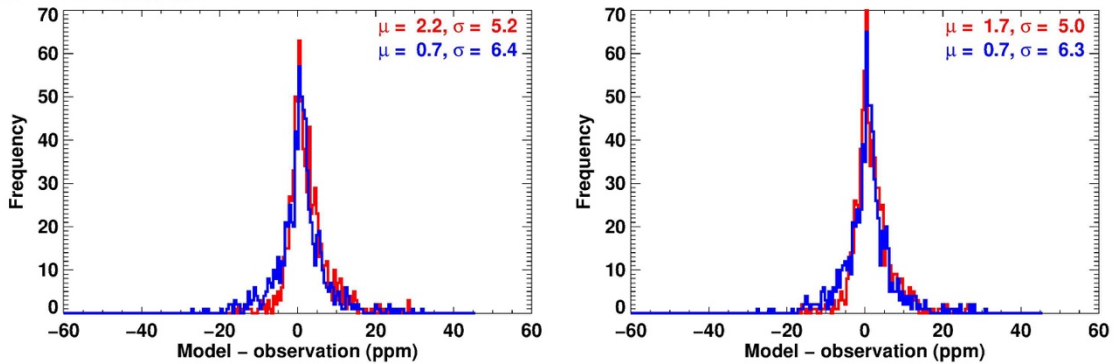


Figure S2. Comparison of model, without and with the chemical pump (left and right panels, respectively) and Amazon aircraft observations over the period of overlap, Jan.-Sep. 2010. Top panels show model-observation difference histograms for the in situ inversions and bottom panels show results for the GOSAT inversions. Mean differences and standard deviations are indicated in the panels.

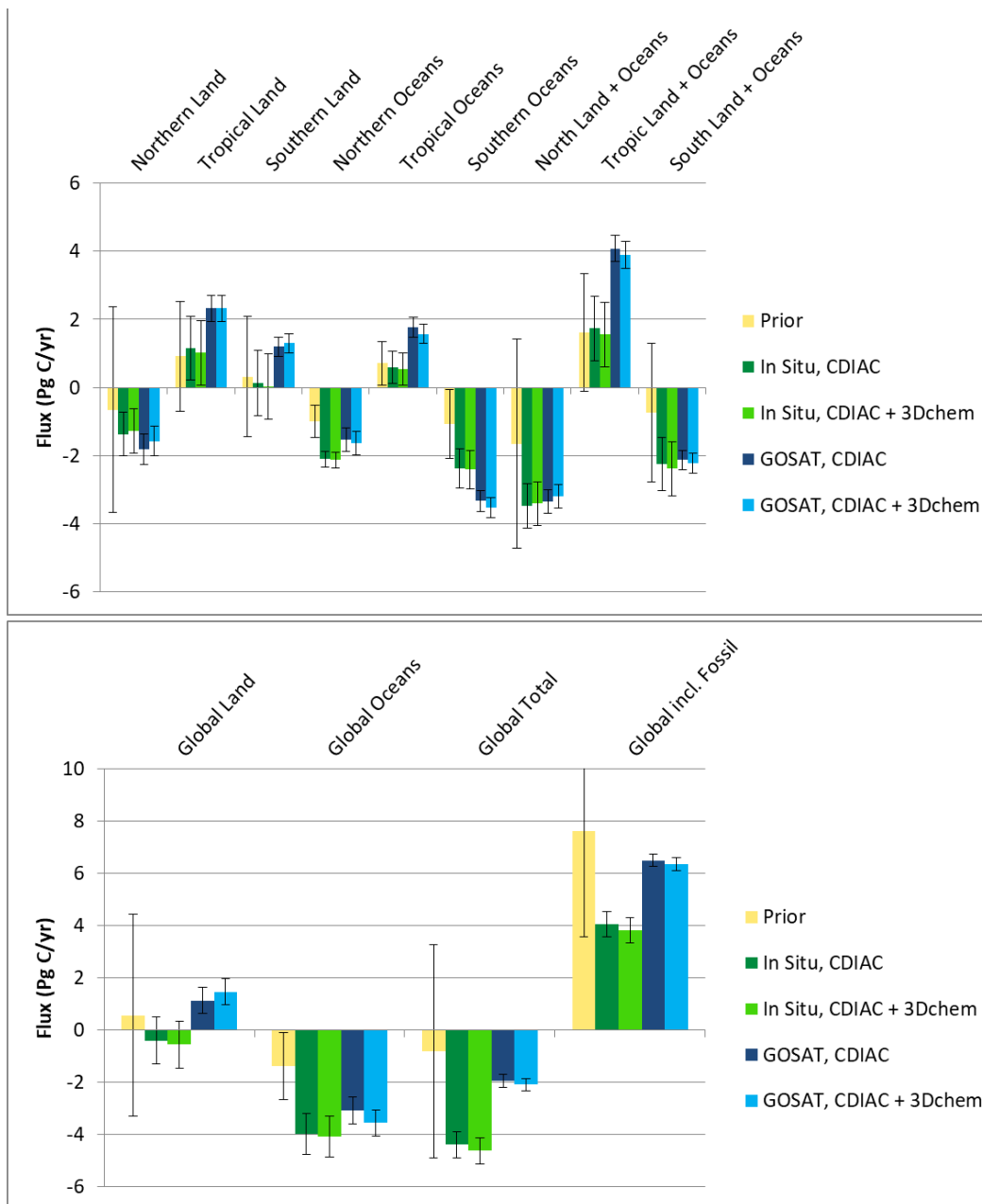


Figure S3. Results for inversions using in situ and GOSAT data with and without the chemical pump and using surface corrections that are more similar to those of previous studies. Note that this set of inversions is based on CDIAC FFCO₂ emissions and does not include international bunkers. Shown are twelve-month (June 2009-May 2010) mean NEP ($\times -1$), fire, and ocean carbon fluxes aggregated over large regions that are defined as in TC3 and in Wang et al. (2018). Error bars represent 1σ uncertainties.